# MEGS$^2$: MEMORY-EFFICIENT GAUSSIAN SPLATTING VIA SPHERICAL GAUSSIANS AND UNIFIED PRUNING

**Jiarui Chen**[1]* **Yikeng Chen**[1,2]* **Yingshuang Zou**[1] **Ye Huang**[3] **Peng Wang**[4]
**Yuan Liu**[1]† **Yujing Sun**[5]† **Wenping Wang**[6]
[1]HKUST [2]SZU [3]SYSU [4]Adobe [5]NTU [6]TAMU


Figure 1: We present **MEGS$^2$**, a memory-efficient framework designed to solve the rendering memory bottleneck of 3D Gaussian Splatting and enable high-quality, real-time rendering on edge devices. As demonstrated in our WebGL-based viewer, 3D Gaussian Splatting(3DGS) with Spherical Harmonics (SH) exhibits low frame rates on desktop GPU and fails to run on mobile platforms. In contrast, MEGS$^2$ achieves interactive frame rates across all tested devices, from desktop to mobile, significantly expanding the applicability of 3DGS.

## ABSTRACT

3D Gaussian Splatting (3DGS) has emerged as a dominant novel-view synthesis technique, but its high memory consumption severely limits its applicability on edge devices. A growing number of 3DGS compression methods have been proposed to make 3DGS more efficient, yet most only focus on storage compression and fail to address the critical bottleneck of rendering memory. To address this problem, we introduce **MEGS$^2$**, a novel memory-efficient framework that tackles this challenge by jointly optimizing two key factors: the total primitive number and the parameters per primitive, achieving unprecedented memory compression. Specifically, we replace the memory-intensive spherical harmonics with lightweight arbitrarily-oriented spherical Gaussian lobes as our color representations. More importantly, we propose a unified soft pruning framework that models primitive-number and lobe-number pruning as a single constrained optimization problem. Experiments show that MEGS$^2$ achieves a 50% static VRAM reduction and a **40%** rendering VRAM reduction compared to existing methods, while maintaining comparable rendering quality.

## 1 INTRODUCTION

Although 3D Gaussian Splatting (3DGS) (Kerbl et al., 2023) has been rapidly replacing implicit neural radiance fields (NeRF) (Mildenhall et al., 2020) as the dominant paradigm in neural rendering—thanks to its fast reconstruction, real-time performance, and high-quality outputs—supporting

*Equal contribution.
†Corresponding authors

its application across devices with varying constraints has become increasingly important. As a result, compression of 3DGS (Bagdasarian et al., 2025) is gaining significantly more attention, with the goal of enabling real-world use cases on edge devices, such as mobile 3D scanning and previewing, virtual try-on, and real-time rendering in video games.

Nevertheless, existing compression methods only focus on storage compression rather than memory compression. While the former storage compression speeds up the one-time data transfer of 3DGS files, the rendering memory dictates whether the 3DGS rendering process can run smoothly on edge devices. This limits the applicability of 3DGS applications to low-end devices like cell phones. For example, some methods based on neural compression, vector quantization, and hash grid compression (Chen et al., 2024; Girish et al., 2024; Lee et al., 2024) achieve high storage compression rates. However, these methods require decoding the full Gaussian parameters from a compressed state before rendering, even resulting in a larger rendering memory than the 3DGS methods without compression. Another branch of works, i.e., primitive pruning methods (Zhang et al., 2025b; Fang & Wang, 2024), are effective at reducing both storage and rendering memory due to the reduced primitives. However, these pruning methods still need to retain a substantial number of 3D Gaussians for a reasonable rendering quality, which still consumes a large rendering memory. How to further reduce the rendering memory of 3DGS-based rendering methods remains an open question.

In this paper, we observe that the overall memory consumption for 3DGS rendering is intrinsically tied to two key factors: the total primitive count and the parameters per primitive. Thus, we propose a novel framework that simultaneously reduces both factors, rather than only optimizing for the primitive numbers in previous methods Zhang et al. (2025b); Fang & Wang (2024). Specifically, the rendering VRAM can be divided into a static component and a dynamic component. The static part relates directly to the total number of Gaussian primitives loaded into the renderer, which is a product of the primitive count and the parameters per primitive. On the other hand, the dynamic part, which consists of intermediate data like projected 2D Gaussian parameters and the tile-depth-gaussian key-value table, is also related to the primitive count in the specific camera viewpoint. This inherent relationship underscores that to reduce the overall memory footprint, we need to reduce both the number of primitives and the per-primitive parameter size.

Based on this analysis, we conclude that to truly address the memory bottleneck, we must reduce both the number of primitives and the number of parameters per primitive. To this end, we first analyze the limitations of using Spherical Harmonics (SH) for color representation. While effective for low-frequency lighting, SH functions are inherently global and require many high-order coefficients to represent localized, high-frequency details like sharp highlights. This results in low parameter utilization and makes them difficult to compress due to the varying parameter counts across different degrees. Building upon this, we introduce the use of Spherical Gaussians (SG) as a more memory-efficient alternative. Spherical Gaussians excel at modeling view-dependent signals with very few parameters, and their complexity can be flexibly controlled by the number of lobes. This inherent locality and sparsity make them a much more convenient and effective choice for compression.

Based on the SG-based representation, we further introduce a novel unified soft pruning framework. We leverage the favorable properties of Spherical Gaussians to dynamically prune redundant lobes for each primitive, thereby compressing the per-primitive parameter count. To achieve a globally optimal memory footprint, our framework models the two traditionally separate pruning problems—primitive-count pruning and per-primitive lobe pruning—as a single constrained optimization problem, with the total parameter budget serving as a unified constraint. Extensive experiments demonstrate that the proposed MEGS$^2$ achieves an excellent balance between rendering quality and VRAM efficiency.

Overall, our contributions can be summarized as follows:

- We introduce a novel color representation for 3DGS by replacing spherical harmonics with arbitrarily-oriented spherical Gaussians, which significantly reduces the per-primitive parameter count and thus lowers rendering VRAM with minimal impact on quality.
- We propose a unified soft pruning framework that models both primitive-count and lobe-pruning as a memory-constrained optimization problem, which yields superior performance compared to existing staged or hard-pruning methods.
- We achieve unprecedented memory compression for 3DGS, surpassing both vanilla and state-of-the-art lightweight methods. Our method delivers over an $\mathbf{8}\times$ static VRAM com-

pression and nearly a **6**× rendering VRAM compression compared to vanilla 3DGS, while maintaining or even improving rendering quality. Furthermore, it still achieves a **2**× static VRAM compression and a 40% rendering VRAM reduction over the SOTA method, GaussianSpa, with comparable quality.

## 2 Related work

### 2.1 Evolution of Splatting-Based Scene Representations

While Neural Radiance Fields (NeRF) (Mildenhall et al., 2020) and their variants (Barron et al., 2021; Müller et al., 2022; Barron et al., 2023) achieved excellent quality in novel view synthesis, their slow rendering speeds precluded real-time applications. 3D Gaussian Splatting (3DGS) (Kerbl et al., 2023) overcame this limitation by introducing a differentiable rasterizer for 3D Gaussians, enabling unprecedented real-time performance with high visual fidelity. The success of 3DGS, however, highlighted its primary challenge: a substantial memory and storage footprint. This has directly motivated the body of work on 3DGS compression and pruning that we discuss subsequently.

### 2.2 Memory Analysis in 3DGS Rendering

In most 3DGS compression studies (Bagdasarian et al., 2025), the rendering memory footprint has not been thoroughly analyzed or compared. Memory usage can be conceptualized into two main components: a static portion, consisting of the total parameters of all loaded Gaussian primitives, and a dynamic portion, representing the runtime overhead. The dynamic overhead, which is highly dependent on a renderer's implementation, includes the storage of preprocessed 2D Gaussian attributes—an overhead that scales significantly with the number of rendering channels, as seen in multi-channel applications like Feature Splatting (Qiu et al., 2024). Additionally, it includes data structures required by tile-based renderers, an overhead first discussed and optimized by FlashGS (Feng et al., 2024) for large-scale scenes.

### 2.3 Pruning Techniques for 3DGS

Pruning unimportant primitives is a natural and widely explored approach for 3DGS compression. Some work has focused on refining adaptive density control strategies to achieve more efficient representations (Kheradmand et al., 2025; Cheng et al., 2024; Liu et al., 2024a; Pateux et al., 2025; Mallick et al., 2024; Kim et al., 2024). Other research has concentrated on defining better importance metrics to decide which primitives to remove, with notable examples including LP-3DGS (Zhang et al., 2024), mini-splatting (Fang & Wang, 2024), and Reduced3DGS (Papantonakis et al., 2024), the latter of which also involves spherical harmonic pruning. A recent noteworthy development is GaussianSpa (Zhang et al., 2025b), which models pruning as a constrained optimization problem, offering a novel perspective and good compatibility with other pruning techniques. While effective at reducing the number of primitives, these methods generally achieve a limited compression ratio and are therefore often used as an initial step within a larger, integrated compression pipeline.

### 2.4 Other Compression Schemes for 3DGS

Besides pruning, researchers have applied common compression techniques like vector quantization, scalar quantization, neural, and hash grid compression to 3DGS (Girish et al., 2024; Lee et al., 2024; Wang et al., 2024a; Lee et al., 2025; Liu et al., 2024b; Navaneet et al., 2024; Xie et al., 2024). While methods with entropy encoding (Chen et al., 2024; 2025; Liu et al., 2025; Wang et al., 2024c) achieve the highest storage compression ratios, they are often limited to structured (anchor-based) Gaussian representations (Lu et al., 2023; Ren et al., 2024; Zhang et al., 2025a). These techniques may drastically reduce file size, but they fail to deliver a comparable reduction in rendering memory. This is because they cannot render directly from a compressed state; instead, they must first decode the full Gaussian parameters. The resulting memory footprint is, therefore, never smaller than that required for uncompressed Gaussian primitives, and the decoding process itself, particularly when involving neural networks, can introduce significant additional memory overhead.

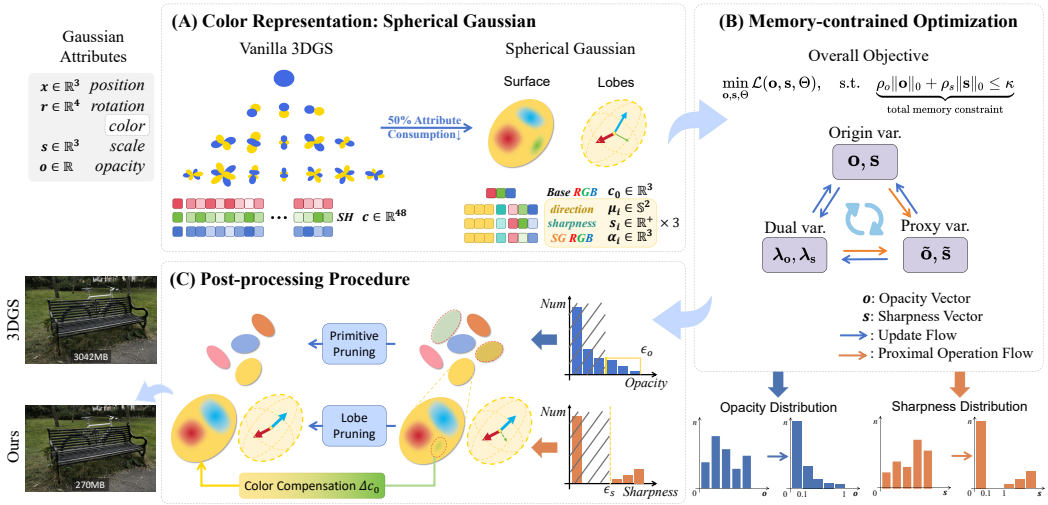


Figure 2: **The detailed architecture of our proposed MEGS$^2$.** (A) In Section 3.2, we first replace the memory-intensive Spherical Harmonics (SH) with Spherical Gaussian (SG) representation. (B) In Section 3.3.1, we formulate the compression as a memory-constrained optimization problem(Eq.6), which is solved using an ADMM-inspired approach (Section 3.3.2) that jointly adjusts primitive opacity and lobe sharpness to progressively sparsify both the number of primitives and the lobes. (C) In Section 3.3.3, primitives and lobes with near-zero opacity and sharpness are removed, and a color compensation term (Eq.15) is introduced to recover the energy of the removed lobes, thereby maintaining rendering quality with a significantly smaller memory consumption.

# 3 METHOD

We present MEGS$^2$, **M**emory-**E**fficient **G**ausian **S**platting via **S**pherical **G**aussian and Unified Pruning, a novel Gaussian compression framework designed from a VRAM-centric perspective. Our method achieves an optimal balance between rendering quality and memory footprint by simultaneously optimizing both the number of Gaussian primitives and the average parameters per primitive.

**Overview** Our pipeline (Fig.2) begins with standard 3DGS initialization and densification. To reduce the parameter count, we introduce a novel color representation for 3DGS by fully replacing spherical harmonics (SH) with spherical Gaussians (SG) (Section 3.2). The core of our approach is a unified soft pruning framework (Section 3.3). This framework treats VRAM compression as a constrained optimization problem, adjusting primitive opacities and lobe sharpness progressively. After this process, a final post-processing step removes near-invalid primitives and low-sharpness lobes to yield a highly compact set of Gaussian primitives that enables rendering with a significantly reduced VRAM footprint.

## 3.1 PRELIMINARIES FOR 3D GAUSSIAN SPLATTING

**Modeling** 3D Gaussian Splatting (3DGS) (Kerbl et al., 2023) represents a scene using a collection of point-based 3D continuous Gaussian primitives. Each primitive is defined by its center position $\mu \in \mathbb{R}^3$, a positive definite covariance matrix $\Sigma \in \mathbb{R}^{3\times3}$, a global opacity $o$, and a view-dependent color model. The covariance matrix is structured as $\Sigma = RSS^\top R^\top$ to ensure its positive definiteness, where $R$ is a rotation matrix and $S$ is a scaling matrix. The view-dependent color is abstractly defined as a function

$$c(\mathbf{v}) : \mathbb{S}^2 \to \mathbb{R}^3, \tag{1}$$

which maps a viewing direction $\mathbf{v}$ from the unit sphere $\mathbb{S}^2$ to an RGB color in $\mathbb{R}^3$.

**Render Pipeline** To render an image from a specific viewpoint, each primitive is projected onto the 2D image plane. The 2D projected covariance matrix $\Sigma'$ is computed via $\Sigma' = JW\Sigma W^\top J^\top$, where $W$ represents the view transformation and $J$ is the Jacobian of the affine approximation of the projective transformation. The final pixel color $C$ is then calculated by blending all projected

primitives that contribute to that pixel in a front-to-back order. The blending process is defined as:

$$C = \sum_{i \in N} c_i \alpha_i \prod_{j=1}^{i-1} (1 - \alpha_j), \tag{2}$$

where $c_i$ is the view-dependent color and $\alpha_i$ is the rendering opacity of the $i$-th primitive. This rendering opacity is determined by the primitive's global opacity $o_i$ and the value of its projected 2D Gaussian at the pixel location. Specifically, the rendering opacity $\alpha_i$ is calculated as:

$$\alpha_i = o_i \cdot \exp\left( -\frac{1}{2} (\mathbf{x} - \mu_i')^\top (\Sigma_i')^{-1} (\mathbf{x} - \mu_i') \right), \tag{3}$$

where $\mathbf{x} \in \mathbb{R}^2$ is the pixel coordinate, $\mu_i' \in \mathbb{R}^2$ is the 2D projected mean, and $\Sigma_i' \in \mathbb{R}^{2\times2}$ is the 2D projected covariance matrix. The view-dependent color $c_i$ is a function of the viewing direction $\mathbf{v}$, commonly modeled using Spherical Harmonics (SH) coefficients.

### 3.2 Spherical Gaussians

Although the original 3D Gaussian Splatting (3DGS) utilized Spherical Harmonics (SH) for color modeling, as we discussed in Section 1, SH functions suffer from limitations in parameter efficiency and the ability to model local and high-frequency signals.

In contrast, Spherical Gaussians (SG) offer a more compact representation, where the parameter count can be controlled by adjusting the number of lobes. As we demonstrated in Figure 3, a three-lobe SG requires only about half the parameters of a 3rd-order SH while achieving comparable expressive power and superior high-frequency detail capture because, in most cases, we only need to model highlights. Furthermore, as shown in Table 4, SG is more amenable to pruning than SH.

SG was first introduced in real-time rendering to support all-frequency shadows from both point lights and environment lights (Wang et al., 2009). Specifically, a lobe of SG has the form

$$G(\mathbf{v}; \mu, s, a) = a e^{s(\mu \cdot \mathbf{v} - 1)}, \tag{4}$$

where $\mu \in \mathbb{S}^2$ is the unit-length lobe axis, $s \in \mathbb{R}^+$ controls the sharpness, and $a \in \mathbb{R}^3$ is the RGB amplitude vector, with $\mathbf{v} \in \mathbb{S}^2$ being the viewing direction.

We use the sum of all lobes of SG for color modeling and introduce a diffuse term to model the direction-independent component. The view-dependent color $c(\mathbf{v})$ is thus computed as:

$$c(\mathbf{v}) = c_0 + \sum_{i=1}^{n} G(\mathbf{v}; \mu_i, s_i, a_i). \tag{5}$$

Where $c(\mathbf{v}) \in \mathbb{R}^3$ is the final color from the viewing direction $\mathbf{v} \in \mathbb{S}^2$, $c_0 \in \mathbb{R}^3$ is the direction-independent diffuse color, and the sum is over $n$ all lobes of SG, with $\mu_i \in \mathbb{S}^2$ being the lobe axis, $s_i \in \mathbb{R}^+$ the sharpness, and $a_i \in \mathbb{R}^3$ the RGB amplitude for the $i$-th spherical lobe.

**Choice of arbitrarily-oriented SG lobes** It is particularly notable that the lobe axes of different SG are not constrained to be orthogonal, nor is any regularization term introduced to enforce orthogonality. Instead, each SG lobe is allowed to have an arbitrary direction. This flexibility grants the SG model a higher degree of freedom, leading to greater representation capability compared to models with fixed orthogonal axes. As shown in Figure 3, SG-Splatting (Wang et al., 2024b) with fixed orthogonal axes demonstrated significant rendering performance degradation, further underscoring the importance of supporting arbitrarily oriented SG lobes.

### 3.3 Unified soft-pruning framework

Benefiting from the property of Spherical Gaussians to control the number of parameters with the number of lobes, they provide an ideal object for pruning. Given that most Gaussian primitives in a scene require only a few lobes to effectively model their color, and that the number of Gaussian primitives is itself often redundant, we propose a novel unified soft pruning framework. In the framework, we first redefine the pruning of both Gaussian primitives and spherical lobes as a unified

optimization problem with a total memory-overhead constraint (Section 3.3.1). To handle the non-differentiable nature of this constraint, we introduce an ADMM-inspired algorithm to efficiently solve the problem (Section 3.3.2). After optimization, the model enters a post-processing procedure where the final primitives and spherical lobes are removed, with rendering quality subsequently recovered through a color compensation strategy and minor fine-tuning (Section 3.3.3).

### 3.3.1 PROBLEM FORMULATION

We unify primitive count pruning and spherical lobe pruning into a memory-constrained optimization problem. The $L_0$ norm of the opacity vector represents the number of active primitives, as Gaussian primitives with zero opacity make no contribution to rendering. Similarly, the $L_0$ norm of the sharpness vector denotes the number of active spherical lobes, since lobes with zero sharpness exhibit no view-dependent effect and their color can be directly added to the diffuse term $c_0$. Building upon GaussianSpa (Zhang et al., 2025b)'s sparsification framework and insights from our analysis, we extend the pruning objective from primitive count optimization to total memory budget control, formalized as:

$$\min_{\mathbf{o},\mathbf{s},\Theta} \mathcal{L}(\mathbf{o},\mathbf{s},\Theta), \quad \text{s.t.} \quad \underbrace{\rho_o\|\mathbf{o}\|_0 + \rho_s\|\mathbf{s}\|_0 \le \kappa}_{\text{total memory constraint}} \tag{6}$$

where $\mathbf{o} \in \mathbb{R}^{N\times 1}$ means opacity vector for $N$ Gaussian primitives, $\mathbf{s} \in \mathbb{R}^{N\times 3}$ means flattened sharpness vector for $N$ Gaussians, $\Theta \in \mathbb{R}^{N\times 13}$ (other Gaussian variables), $\rho_o = 11$ and $\rho_s = 7$ count base parameters for a single Gaussian primitive and a single SG lobe respectively, and $\kappa$ is the total parameter budget. $\mathcal{L}(\mathbf{o},\mathbf{s},\Theta)$ is the reconstruction loss function.

### 3.3.2 MEMORY-CONSTRAINED OPTIMIZATION

In this subsection, we aim to solve the memory-constrained optimization defined in Section 3.3.1. Due to the introduction of a non-differentiable component (the $L_0$ norm) into the constraint, we cannot directly optimize it with regularized stochastic gradient descent. Instead, we adopt an ADMM-inspired approach by introducing proxy variables $\tilde{\mathbf{o}}$ and $\tilde{\mathbf{s}}$ for $\mathbf{o}$ and $\mathbf{s}$, respectively. This decomposition strategy enables us to split the original optimization problem into two tractable subproblems:

$$\min_{\mathbf{o},\mathbf{s},\Theta} \mathcal{L}(\mathbf{o},\mathbf{s},\Theta) + \frac{\delta}{2}\left(\rho_o\|\mathbf{o}-\tilde{\mathbf{o}}+\boldsymbol{\lambda}_\mathbf{o}\|^2 + \rho_s\|\mathbf{s}-\tilde{\mathbf{s}}+\boldsymbol{\lambda}_\mathbf{s}\|^2\right) \tag{7}$$

$$\min_{\tilde{\mathbf{o}},\tilde{\mathbf{s}}} h(\tilde{\mathbf{o}},\tilde{\mathbf{s}}) + \frac{\delta}{2}\left(\rho_o\|\mathbf{o}-\tilde{\mathbf{o}}+\boldsymbol{\lambda}_\mathbf{o}\|^2 + \rho_s\|\mathbf{s}-\tilde{\mathbf{s}}+\boldsymbol{\lambda}_\mathbf{s}\|^2\right) \tag{8}$$

where $h(\cdot,\cdot)$ is an indicator function enforcing the sparsity constraint:

$$h(\mathbf{o},\mathbf{s}) = \begin{cases} 0 & \text{if } \rho_o\|\mathbf{o}\|_0 + \rho_s\|\mathbf{s}\|_0 \le \kappa, \\ +\infty & \text{otherwise} \end{cases} \tag{9}$$

and the proxy variables are updated via the proximal operator:

$$(\tilde{\mathbf{o}},\tilde{\mathbf{s}}) = \mathbf{prox}_h(\mathbf{o}+\boldsymbol{\lambda}_\mathbf{o}, \mathbf{s}+\boldsymbol{\lambda}_\mathbf{s}). \tag{10}$$

Here, $\boldsymbol{\lambda}_\mathbf{o}$ and $\boldsymbol{\lambda}_\mathbf{s}$ denote the corresponding Lagrange multipliers for the constraints.

The specific algorithm flow can be found in Algorithm 1.

**Proximal Operator Implementation** The proximal operator projects $\mathbf{o}$ and $\mathbf{s}$ onto the constraint $\rho_1\|\mathbf{o}\|_0 + \rho_2\|\mathbf{s}\|_0 \le \kappa$, compatible with any importance metric. To simplify the design and leverage importance criteria from prior primitive-pruning research, we choose to factorize the projection:

$$\tilde{\mathbf{o}} = \mathbf{prox}_h(\mathbf{o}+\boldsymbol{\lambda}_\mathbf{o}), \|\tilde{\mathbf{o}}\|_0 < \kappa_\mathbf{o} \tag{11}$$

$$\tilde{\mathbf{s}} = \mathbf{prox}_h(\mathbf{s}+\boldsymbol{\lambda}_\mathbf{s}), \|\tilde{\mathbf{s}}\|_0 < \kappa_\mathbf{s} \tag{12}$$

**Algorithm 1** Memory-constrained optimizing

**Require:**
Initial parameters: $\Theta^0$, $\mathbf{o}^0$, $\mathbf{s}^0$
Proxy variables: $\tilde{\mathbf{o}}^0 = \mathbf{o}^0$, $\tilde{\mathbf{s}}^0 = \mathbf{s}^0$
Dual variables: $\boldsymbol{\lambda}_\mathbf{o}^0 = \mathbf{0}$, $\boldsymbol{\lambda}_\mathbf{s}^0 = \mathbf{0}$
Learning rate $\eta$, penalty $\delta$, budget $\kappa$
**Ensure:**
Optimized parameters: $\Theta^K$, $\mathbf{o}^K$, $\mathbf{s}^K$
**for** $k = 0$ **to** $K - 1$ **do**
  **Gradient Step:**
  $\Theta^{k+1} \leftarrow \Theta^k - \eta \nabla_\Theta \mathcal{L}(\Theta^k, \mathbf{o}^k, \mathbf{s}^k)$
  $\mathbf{o}^{k+1} \leftarrow \mathbf{o}^k - \eta \left[\nabla_\mathbf{o} \mathcal{L}(\Theta^k, \mathbf{o}^k, \mathbf{s}^k) + \delta(\mathbf{o}^k - \tilde{\mathbf{o}}^k + \boldsymbol{\lambda}_\mathbf{o}^k)\right]$
  $\mathbf{s}^{k+1} \leftarrow \mathbf{s}^k - \eta \left[\nabla_\mathbf{s} \mathcal{L}(\Theta^k, \mathbf{o}^{k+1}, \mathbf{s}^k) + \delta(\mathbf{s}^k - \tilde{\mathbf{s}}^k + \boldsymbol{\lambda}_\mathbf{s}^k)\right]$
  **Proximal Step:**
  $(\tilde{\mathbf{o}}^{k+1}, \tilde{\mathbf{s}}^{k+1}) \leftarrow \mathbf{prox}_h(\mathbf{o}^{k+1} + \boldsymbol{\lambda}_\mathbf{o}^k, \mathbf{s}^{k+1} + \boldsymbol{\lambda}_\mathbf{s}^k)$
  **Dual Update:**
  $\boldsymbol{\lambda}_\mathbf{o}^{k+1} \leftarrow \boldsymbol{\lambda}_\mathbf{o}^k + (\mathbf{o}^{k+1} - \tilde{\mathbf{o}}^{k+1})$
  $\boldsymbol{\lambda}_\mathbf{s}^{k+1} \leftarrow \boldsymbol{\lambda}_\mathbf{s}^k + (\mathbf{s}^{k+1} - \tilde{\mathbf{s}}^{k+1})$
**end for**
**Return** $\Theta^K$, $\mathbf{o}^K$, $\mathbf{s}^K$

For opacity projection, Zhang et al. (2025b) has established multiple proximal operators that are selected based on scene characteristics. Our approach reuses these operators.

For sharpness projection, we propose two distinct operators:

- **Sharpness-Based Selection**: Sorts $(\mathbf{s} + \boldsymbol{\lambda}_\mathbf{s})$ and preserves the $\kappa_s$ elements with highest magnitudes, where $\kappa_s$ controls the number of active spherical harmonic coefficients.
- **Range-Based Selection**: Similarly, Retains $\kappa_s$ elements using the dynamic range metric:

$$D_i = |\max_\mathbf{v}(c_i) - \min_\mathbf{v}(c_i)| = |a_i|(1 - e^{-2s_i}) \tag{13}$$

  where $a_i$ is the RGB amplitude for the $i$-th spherical lobe.

**Discussion: Sequential vs. Unified Pruning** While sequential pruning tackles memory reduction in a two-stage process—first reducing primitive count, then per-primitive parameters—our unified framework jointly optimizes both factors as a single problem. This approach finds a better trade-off between primitive count and per-primitive complexity, thus avoiding the sub-optimal solutions often found by sequential methods. For a detailed experimental validation, please refer to Section 4.4.2.

### 3.3.3 Post-Processing Procedure

After completing the constrained optimization process, we obtain a large number of primitives and spherical lobes with near-zero opacity and sharpness values, respectively. As the hard constraints are enforced on the proxy variables rather than the original ones, these near-zero values must still be pruned to achieve an actual memory and storage benefit. We address this with a three-step post-processing strategy: first, we remove Gaussian primitives whose opacity falls below a certain threshold. Then, for spherical lobes, we remove those with negligible sharpness and introduce a simple color compensation method to minimize the average per-view color variation and mitigate performance degradation caused by their removal.

This compensation is achieved by finding an optimal term, $\Delta c_0$, that minimizes the integral of the squared color difference over all view directions on the unit sphere:

$$\min_{\Delta c_0} \int_{\mathbb{S}^2} \left((c_0 + \Delta c_0) - (c_0 + G(\mathbf{v}; \mu_i, s_i, a_i))\right)^2 d\mathbf{v} \tag{14}$$

Solving this optimization problem yields an exact compensation term that preserves the energy of the removed lobe:

$$\Delta c_0 = a_i \cdot \frac{1 - e^{-2s_i}}{2s_i} \tag{15}$$

The diffuse term of the parent primitive is then updated with this value:

$$c_0' = c_0 + \Delta c_0 \tag{16}$$

Finally, after removing some Gaussian primitives and spherical lobes, we continue to fine-tune for a small number of steps to recover the rendering quality.

# 4 EXPERIMENTS

## 4.1 EXPERIMENTAL SETTINGS

**Datasets and Metrics** Following 3DGS (Kerbl et al., 2023), we evaluate the rendering performance on real-world datasets, including all indoor scenes and outdoor scenes in Mip-NeRF360 (Barron et al., 2022), two scenes from Tanks & Temples (Knapitsch et al., 2017), and two scenes from Deep Blending (Hedman et al., 2018). Additionally, we measure the VRAM overhead during the Gaussian loading (static) and rendering stages on these scenes.

**Baselines** On all datasets, we benchmark our method against four categories of baselines: (1) vanilla 3DGS (Kerbl et al., 2023) and SG-Splatting (Wang et al., 2024b); (2) lightweight 3DGS methods based on primitive pruning: LP-3DGS (Zhang et al., 2024), Mini-Splatting (Fang & Wang, 2024), and GaussianSpa (Zhang et al., 2025b); (3) lightweight 3DGS methods based on pruning spherical harmonic coefficients: Reduced3DGS (Papantonakis et al., 2024); (4) 3DGS compression methods utilizing orthogonal techniques such as neural compression and vector quantization: CompactGaussian (Lee et al., 2024), EAGLES (Girish et al., 2024), and MesonGS (Xie et al., 2024).

**Implementation Details** Our experiments are conducted on a single NVIDIA RTX 3090 GPU (24GB). For a fair comparison, we adopt the same hyperparameters and optimizer used by vanilla 3DGS on all datasets. Regarding the training strategy, we employ the same densification, pruning, and fine-tuning procedures as GaussianSpa, conducting densification training, sparse training, and fine-tuning for the same number of steps. To ensure the accuracy of our VRAM measurements, we reproduce 3DGS, GaussianSpa, EAGLES, CompactGaussian, MesonGS, and Reduced3DGS for direct VRAM measurement. For other pruning-based methods, we utilize both the rendering quality metrics and primitive counts reported in the GaussianSpa paper. We then estimate their corresponding VRAM consumption based on our own VRAM measurements for 3DGS and GaussianSpa.

**Evaluation Details** For rendering performance, we report the peak signal-to-noise ratio (PSNR), structural similarity (SSIM), and learned perceptual image patch similarity(LPIPS). For VRAM consumption, we report both static VRAM overhead and rendering VRAM overhead. The former refers to the VRAM required to load all 3DGS primitives into the renderer and dequantize or decode them into a ready-to-render state. This is not necessarily equal to the file size, as some methods might represent Gaussian attributes in a more compact or lower-precision data format but still require restoring them to full, 32-bit precision Gaussian attributes before rendering. The latter denotes the peak VRAM usage during the rendering process, which is typically larger than the static VRAM due to the introduction of intermediate variables (e.g., projected 2D Gaussian attributes, key-value tables for tile-based rendering) during rendering. We measure this value across all test viewpoints and report the average. To exclude the overhead introduced by the framework itself and the impact of memory fragmentation, we note that the memory allocation and management of the official 3DGS implementation's renderer are almost entirely handled by PyTorch. Therefore, all VRAM-related metrics are reported using the values provided by the PyTorch framework.

## 4.2 MAIN RESULTS AND ANALYSIS

The quantitative results are summarized in Table 1, comparing our approach with several existing lightweight 3DGS methods. Overall, our method achieves comparable or slightly superior rendering quality to the current state-of-the-art lightweight 3DGS methods, while demonstrating significantly lower VRAM overhead across all existing methods.

Compared to vanilla 3DGS, our method achieves a 0.4 dB PSNR improvement on the DeepBlending dataset and a 0.012 LPIPS reduction on the Tanks & Temples dataset. Furthermore, it achieves more than an $\mathbf{8}\times$ compression rate for static VRAM and nearly a $\mathbf{6}\times$ compression rate for rendering VRAM across all datasets.

Table 1: **Quantitative comparison across three datasets.** Best results are in red region, second best are in orange region, and third best are in blue region. Memory (VRAM) values are in MB. EAGLES cannot be trained on a single NVIDIA RTX 3090 GPU with 24GB on some scenes in Mip-NeRF360, so we do not report VRAM consumption.

| Method | Mip-NeRF 360 | | | | | Tanks&Temples | | | | | DeepBlending | | | | |
|---|---|---|---|---|---|---|---|---|---|---|---|---|---|---|---|
| | PSNR↑ | SSIM↑ | LPIPS↓ | VRAM↓ Stat. | VRAM↓ Rend. | PSNR↑ | SSIM↑ | LPIPS↓ | VRAM↓ Stat. | VRAM↓ Rend. | PSNR↑ | SSIM↑ | LPIPS↓ | VRAM↓ Stat. | VRAM↓ Rend. |
| 3DGS | 27.48 | 0.813 | 0.217 | 648 | 1717 | 23.68 | 0.849 | 0.171 | 370 | 1021 | 29.71 | 0.902 | 0.242 | 582 | 1569 |
| SG-Splatting | 27.27 | 0.813 | 0.218 | 416 | 1327 | 23.47 | 0.840 | 0.177 | 229 | 822 | 29.57 | 0.901 | 0.247 | 357 | 983 |
| Reduced3DGS | 27.21 | 0.810 | 0.225 | 191 | 493 | 23.51 | 0.839 | 0.187 | 90 | 252 | 29.60 | 0.902 | 0.248 | 121 | 340 |
| CompactGaussian | 27.08 | 0.798 | 0.247 | 267 | 838 | 23.32 | 0.831 | 0.201 | 177 | 469 | 29.79 | 0.901 | 0.258 | 187 | 532 |
| EAGLES | 27.23 | 0.810 | 0.240 | – | – | 23.37 | 0.840 | 0.200 | 333 | 965 | 29.86 | 0.910 | 0.250 | 510 | 1550 |
| MesonGS-FT | 26.98 | 0.801 | 0.233 | 709 | 1336 | 23.32 | 0.837 | 0.193 | 424 | 783 | 29.51 | 0.901 | 0.251 | 656 | 1202 |
| LP-3DGS | 27.12 | 0.805 | 0.239 | 420 | 1239 | 23.41 | 0.834 | 0.198 | 251 | 769 | – | – | – | – | – |
| Mini-Splatting | 27.40 | 0.821 | 0.219 | 125 | 477 | 23.45 | 0.841 | 0.186 | 72 | 253 | 30.05 | 0.909 | 0.254 | 89 | 324 |
| GaussianSpa | 27.56 | 0.824 | 0.215 | 115 | 448 | 23.73 | 0.857 | 0.162 | 106 | 336 | 30.00 | 0.912 | 0.239 | 104 | 372 |
| Ours | 27.54 | 0.824 | 0.209 | 55 | 265 | 23.57 | 0.855 | 0.159 | 59 | 209 | 30.17 | 0.912 | 0.233 | 54 | 243 |
| | 27.21 | 0.814 | 0.227 | 40 | 224 | 23.27 | 0.851 | 0.167 | 37 | 163 | 30.01 | 0.908 | 0.246 | 33 | 193 |

Even when compared to the current state-of-the-art lightweight 3DGS method, GaussianSpa (Zhang et al., 2025b), we still achieve a nearly 2× compression rate for static VRAM on the Mip-NeRF360 dataset and reduce rendering VRAM by approximately 40% with comparable rendering quality.

**Analysis on Existing Compression Methods** It is noteworthy that methods based on vector quantization, neural network compression, or hash grid compression (CompactGaussian (Lee et al., 2024), EAGLES (Girish et al., 2024), MesonGS (Xie et al., 2024), despite achieving high storage compression rates, lack advantages in terms of static and rendering VRAM. We summarize the average parameter costs for the color model of these methods in Table 2. This is because they still cannot render directly from their compressed state in the latent space or codebook space; they must first decode the full Gaussian parameters. This decoding and dequantization overhead results in both their static and rendering VRAM being even higher than that of vanilla 3DGS methods with a similar number of primitives. Similarly, we compare our method against HAC++ (Chen et al., 2025), a state-of-the-art storage compression algorithm only for anchor-based 3DGS on the Mip-NeRF360 dataset. As shown in Table 3, HAC++ does not significantly reduce VRAM compared to its baseline, Scaffold-GS (Lu et al., 2023), because its compressed representation must be fully decompressed for rendering. In contrast, our method demonstrates a clear advantage in metrics closer to human perception (SSIM and LPIPS) while achieving approximately 50-60% lower VRAM overhead and a 1.5-1.7x rendering speedup.

**Analysis on Pruning-based Methods** Pruning-based methods (Zhang et al., 2025b; Fang & Wang, 2024; Zhang et al., 2024), while effectively reducing both static and rendering VRAM, have reached a point where it is difficult to further reduce the number of Gaussian primitives without compromising rendering quality, thus limiting the potential for higher VRAM compression rates. For methods that independently prune primitives and spherical harmonics, such as Reduced3DGS (Papantonakis et al., 2024), our advantage stems from two key factors: the superior pruning amenability of Spherical Gaussians and the more effective, unified soft pruning framework. A detailed discussion and experimental validation of this superiority are provided in Section 4.4.

### 4.3 Qualitative Results

Figure 4 presents a qualitative comparison of our method against baselines, including GaussianSpa and 3DGS on various scenes. In the Bicycle and Truck scenes, our method accurately recovers specular reflections on smooth surfaces and mirrors, details that other methods fail to fully capture. In the Bonsai scene, our approach faithfully captures high-contrast lighting in both contours and brightness. Furthermore, in the Playroom scene, where GaussianSpa struggles with the reconstruction of the wall corner, and 3DGS suffers from a loss of detail in other regions, our method delivers

a cleaner and more complete reconstruction. Notably, our method achieves these high-quality results with a VRAM footprint of only 50-60% compared to GaussianSpa, demonstrating a substantial enhancement in memory efficiency. These visual results indicate that our Spherical Gaussian (SG) based representation has a stronger capability for fitting local view-dependent signals than Spherical Harmonics (SH), leading to sharper and more photorealistic images.

Table 2: **Average parameter costs for the color model per Gaussian primitive.** Storage and Rendering costs are measured in the number of float32 parameters. Decode Overhead indicates whether a method introduces significant additional VRAM during calculating color. The values of our method are calculated on the DeepBlending dataset.

| Method | Storage | Rendering | Decode Overhead |
|---|---|---|---|
| 3DGS | 48 | 48 | No |
| EAGLES | $< 1$ | $> 48$ | Yes |
| CompactGaussian | $< 1$ | $> 32$ | Yes |
| ours w/o lobe-pruning | 24 | 24 | No |
| ours | 9.7 | 9.7 | No |

Table 3: **Comparison of anchor-based 3DGS and specialized SOTA compression schemes** on the Mip-NeRF360 dataset. The best result is shown in **bold**.

| Method | PSNR↑ | SSIM↑ | LPIPS↓ | VRAM↓ | FPS↑ |
|---|---|---|---|---|---|
| Scaffold-GS | 27.74 | 0.811 | 0.226 | 612 | 123 |
| HAC++ (highrate) | **27.81** | 0.811 | 0.231 | 637 | 115 |
| HAC++ (lowrate) | 27.60 | 0.803 | 0.253 | 514 | 132 |
| Ours | 27.54 | **0.824** | **0.209** | **265** | **200** |

Table 4: **Ablation studies for different pruning strategies** on Mip-NeRF360 dataset. Memory (VRAM) values are in MB. The best result is shown in **bold**.

| Method | PSNR↑ | SSIM↑ | LPIPS↓ | VRAM↓ |
|---|---|---|---|---|
| GaussianSpa + Reduce3DGS | 26.05 | 0.776 | 0.280 | 402 |
| GaussianSpa (SH → SG) | 27.01 | 0.808 | 0.230 | 339 |
| Ablation 1: soft → hard | 27.23 | 0.814 | 0.228 | 288 |
| Ablation 2: unified → sequential | 27.33 | 0.818 | 0.222 | 328 |
| Ablation 3: w/o color compensation | 27.46 | 0.822 | 0.213 | **265** |
| Unified soft pruning (ours full) | **27.54** | **0.824** | **0.209** | **265** |

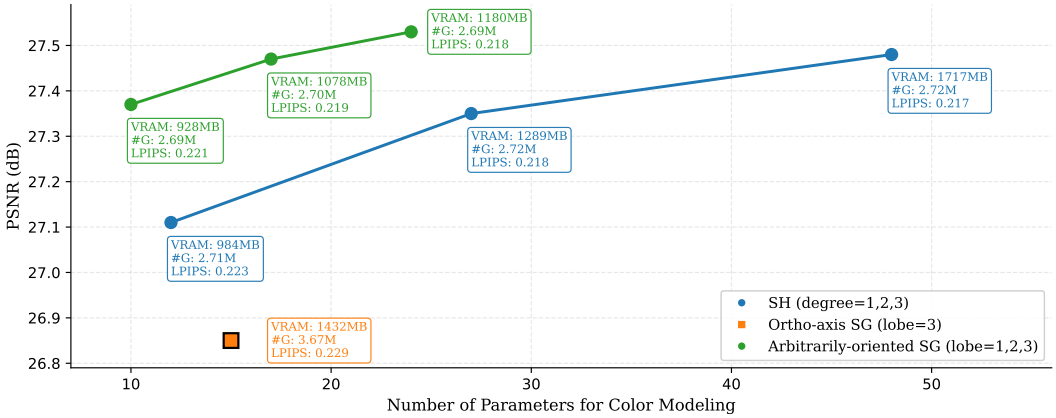


Figure 3: Comparison of different 3DGS color representations on Mip-NeRF360 dataset.


Figure 4: Qualitative results on the Bicycle, Bonsai, Kitchen, Playroom and Truck scenes comparing to previous methods and the corresponding ground truth images from test views. The rendering VRAM consumption for the corresponding method is annotated at the bottom of each image.

### 4.4 Ablation Studies

In this section, we conduct a series of ablation studies to validate the effectiveness of our proposed designs and answer two key questions:

1. Is the replacement of spherical harmonics with spherical Gaussians necessary? And why not use the theoretically lighter-weight orthogonal-axis spherical variants? (Section 4.4.1)
2. Is our proposed unified soft pruning framework effective? And does it offer a significant advantage over simply combining existing pruning methods? (Section 4.4.2)

#### 4.4.1 Ablation on Color Modeling

To directly evaluate the effectiveness of our color modeling, we replace spherical harmonics (SH) in vanilla 3DGS with our arbitrarily-oriented spherical Gaussians (SG). We ensure a fair comparison by using identical hyperparameters and training strategies. As shown in Figure 3, our SG-based model achieves either higher quality with similar VRAM usage or comparable quality with significantly less VRAM compared to SH-based approaches.

Furthermore, we compare our arbitrarily-oriented SG to the orthogonal-axis SG proposed in SG-Splatting (Wang et al., 2024b). Although theoretically more lightweight, the fixed-axis variant suffers a significant drop in rendering quality (about 0.6 dB PSNR) as it cannot efficiently capture complex view-dependent effects. This also makes it unsuitable for lobe-pruning, as view-dependent effects cannot be guaranteed to align with its predefined axes.

#### 4.4.2 Ablation on Pruning Strategies

To evaluate the efficacy of our unified soft pruning framework, we compare our final method with key ablation variants. First, we examine a version that ablates our lobe soft pruning, denoted as "Ablation 1: soft $\rightarrow$ hard" , which only performs constrained optimization on opacity, rather than on both opacity and sharpness. As shown in Table 4, the lack of a sharpness adjustment stage leads to an irreversible drop in performance when lobes are removed.

Next, we evaluate a variant that performs primitive and lobe pruning independently (sequential pruning), denoted as "Ablation 2: unified $\rightarrow$ sequential". This sequential approach is inferior to our final unified method, which achieves a better rendering quality and VRAM trade-off. As we discussed in Section 3.3.2, this underscores the fundamental advantage of our unified framework. We have also experimentally validated the effectiveness of the introduced color compensation mechanism.

Finally, we compare our framework to two simple baselines to demonstrate that a naive combination of existing techniques is insufficient to achieve our goal. The first, which combines the SOTA pruning method GaussianSpa (Zhang et al., 2025b) with the spherical harmonics coefficient pruning of Reduced3DGS (Papantonakis et al., 2024), shows a severe rendering quality degradation (Table 4). This highlights the failure of existing spherical harmonics pruning metrics when applied to a reduced number of Gaussian primitives, which further validates our discussion on the limitations of spherical harmonics in Section 1. The second baseline, which replaces the spherical harmonics in GaussianSpa with spherical Gaussians, performs worse than our method in both memory footprint and rendering quality. This demonstrates that our pruning strategy not only reduces memory but also acts as a regularizer, improving rendering quality on novel views.

## 5 LIMITATION

Our current compression framework primarily focuses on static memory consumption to ensure generalizability across various rendering platforms and implementations. The dynamic portion of VRAM, which is highly dependent on specific renderer configurations (e.g., the tile-depth-Gaussian key-value table in a tile-based CUDA renderer), was not integrated into our framework as this remains a promising direction for future research. Furthermore, the ability of our framework to accurately model highlights with particularly complex or intricate shapes warrants more comprehensive testing and discussion.

## 6 CONCLUSION

In this paper, we introduced MEGS$^2$, a novel framework that fundamentally solves the memory bottleneck of 3D Gaussian Splatting by jointly optimizing both primitive count and per-primitive parameters. Our approach pioneers a lightweight spherical Gaussian representation for color and a unified soft pruning method, which together deliver unprecedented memory compression. Our framework establishes a new paradigm for 3DGS compression by prioritizing rendering VRAM efficiency, a critical step towards enabling high-quality neural rendering on the edge.

## REFERENCES


Milena T. Bagdasarian, Paul Knoll, Yi-Hsin Li, Florian Barthel, Anna Hilsmann, Peter Eisert, and Wieland Morgenstern. 3dgs.zip: A survey on 3d gaussian splatting compression methods, 2025. URL https://arxiv.org/abs/2407.09510.

Jonathan T. Barron, Ben Mildenhall, Matthew Tancik, Peter Hedman, Ricardo Martin-Brualla, and Pratul P. Srinivasan. Mip-nerf: A multiscale representation for anti-aliasing neural radiance fields, 2021. URL https://arxiv.org/abs/2103.13415.

Jonathan T. Barron, Ben Mildenhall, Dor Verbin, Pratul P. Srinivasan, and Peter Hedman. Mip-nerf 360: Unbounded anti-aliased neural radiance fields. *CVPR*, 2022.

Jonathan T. Barron, Ben Mildenhall, Dor Verbin, Pratul P. Srinivasan, and Peter Hedman. Zip-nerf: Anti-aliased grid-based neural radiance fields, 2023. URL https://arxiv.org/abs/2304.06706.

Yihang Chen, Qianyi Wu, Weiyao Lin, Mehrtash Harandi, and Jianfei Cai. Hac: Hash-grid assisted context for 3d gaussian splatting compression, 2024. URL https://arxiv.org/abs/2403.14530.

Yihang Chen, Qianyi Wu, Weiyao Lin, Mehrtash Harandi, and Jianfei Cai. Hac++: Towards 100x compression of 3d gaussian splatting, 2025. URL https://arxiv.org/abs/2501.12255.

Kai Cheng, Xiaoxiao Long, Kaizhi Yang, Yao Yao, Wei Yin, Yuexin Ma, Wenping Wang, and Xuejin Chen. Gaussianpro: 3d gaussian splatting with progressive propagation, 2024. URL https://arxiv.org/abs/2402.14650.

Guangchi Fang and Bing Wang. Mini-splatting: Representing scenes with a constrained number of gaussians, 2024. URL https://arxiv.org/abs/2403.14166.

Guofeng Feng, Siyan Chen, Rong Fu, Zimu Liao, Yi Wang, Tao Liu, Zhilin Pei, Hengjie Li, Xingcheng Zhang, and Bo Dai. Flashgs: Efficient 3d gaussian splatting for large-scale and high-resolution rendering, 2024. URL https://arxiv.org/abs/2408.07967.

Sharath Girish, Kamal Gupta, and Abhinav Shrivastava. Eagles: Efficient accelerated 3d gaussians with lightweight encodings, 2024. URL https://arxiv.org/abs/2312.04564.

Peter Hedman, Julien Philip, True Price, Jan-Michael Frahm, George Drettakis, and Gabriel Brostow. Deep blending for free-viewpoint image-based rendering. 37(6):257:1–257:15, 2018.

Bernhard Kerbl, Georgios Kopanas, Thomas Leimkühler, and George Drettakis. 3d gaussian splatting for real-time radiance field rendering. *ACM Transactions on Graphics*, 42(4), July 2023. URL https://repo-sam.inria.fr/fungraph/3d-gaussian-splatting/.

Shakiba Kheradmand, Daniel Rebain, Gopal Sharma, Weiwei Sun, Jeff Tseng, Hossam Isack, Abhishek Kar, Andrea Tagliasacchi, and Kwang Moo Yi. 3d gaussian splatting as markov chain monte carlo, 2025. URL https://arxiv.org/abs/2404.09591.

Sieun Kim, Kyungjin Lee, and Youngki Lee. Color-cued efficient densification method for 3d gaussian splatting. In *Proceedings of the IEEE/CVF Conference on Computer Vision and Pattern Recognition (CVPR) Workshops*, pp. 775–783, June 2024.

Arno Knapitsch, Jaesik Park, Qian-Yi Zhou, and Vladlen Koltun. Tanks and temples: Benchmarking large-scale scene reconstruction. *ACM Transactions on Graphics*, 36(4), 2017.

Joo Chan Lee, Daniel Rho, Xiangyu Sun, Jong Hwan Ko, and Eunbyung Park. Compact 3d gaussian representation for radiance field. In *Proceedings of the IEEE/CVF Conference on Computer Vision and Pattern Recognition (CVPR)*, pp. 21719–21728, 2024.

Soonbin Lee, Fangwen Shu, Yago Sanchez, Thomas Schierl, and Cornelius Hellge. Compression of 3d gaussian splatting with optimized feature planes and standard video codecs, 2025. URL https://arxiv.org/abs/2501.03399.

Lei Liu, Zhenghao Chen, Wei Jiang, Wei Wang, and Dong Xu. Hemgs: A hybrid entropy model for 3d gaussian splatting data compression, 2025. URL https://arxiv.org/abs/2411.18473.

Rong Liu, Rui Xu, Yue Hu, Meida Chen, and Andrew Feng. Atomgs: Atomizing gaussian splatting for high-fidelity radiance field, 2024a. URL https://arxiv.org/abs/2405.12369.

Xiangrui Liu, Xinju Wu, Pingping Zhang, Shiqi Wang, Zhu Li, and Sam Kwong. Compgs: Efficient 3d scene representation via compressed gaussian splatting, 2024b. URL https://arxiv.org/abs/2404.09458.

Tao Lu, Mulin Yu, Linning Xu, Yuanbo Xiangli, Limin Wang, Dahua Lin, and Bo Dai. Scaffold-gs: Structured 3d gaussians for view-adaptive rendering, 2023. URL https://arxiv.org/abs/2312.00109.

Saswat Subhajyoti Mallick, Rahul Goel, Bernhard Kerbl, Francisco Vicente Carrasco, Markus Steinberger, and Fernando De La Torre. Taming 3dgs: High-quality radiance fields with limited resources, 2024. URL https://arxiv.org/abs/2406.15643.

Ben Mildenhall, Pratul P. Srinivasan, Matthew Tancik, Jonathan T. Barron, Ravi Ramamoorthi, and Ren Ng. Nerf: Representing scenes as neural radiance fields for view synthesis, 2020. URL https://arxiv.org/abs/2003.08934.

Thomas Müller, Alex Evans, Christoph Schied, and Alexander Keller. Instant neural graphics primitives with a multiresolution hash encoding. *ACM Transactions on Graphics*, 41(4):1–15, July 2022. ISSN 1557-7368. doi: 10.1145/3528223.3530127. URL http://dx.doi.org/10.1145/3528223.3530127.

KL Navaneet, Kossar Pourahmadi Meibodi, Soroush Abbasi Koohpayegani, and Hamed Pirsiavash. Compgs: Smaller and faster gaussian splatting with vector quantization, 2024. URL https://arxiv.org/abs/2311.18159.

Panagiotis Papantonakis, Georgios Kopanas, Bernhard Kerbl, Alexandre Lanvin, and George Drettakis. Reducing the memory footprint of 3d gaussian splatting. *Proceedings of the ACM on Computer Graphics and Interactive Techniques*, 7(1), May 2024. URL https://repo-sam.inria.fr/fungraph/reduced_3dgs/.

Stéphane Pateux, Matthieu Gendrin, Luce Morin, Théo Ladune, and Xiaoran Jiang. Bogauss: Better optimized gaussian splatting, 2025. URL https://arxiv.org/abs/2504.01844.

Ri-Zhao Qiu, Ge Yang, Weijia Zeng, and Xiaolong Wang. Feature splatting: Language-driven physics-based scene synthesis and editing, 2024. URL https://arxiv.org/abs/2404.01223.

Kerui Ren, Lihan Jiang, Tao Lu, Mulin Yu, Linning Xu, Zhangkai Ni, and Bo Dai. Octree-gs: Towards consistent real-time rendering with lod-structured 3d gaussians, 2024. URL https://arxiv.org/abs/2403.17898.

Henan Wang, Hanxin Zhu, Tianyu He, Runsen Feng, Jiajun Deng, Jiang Bian, and Zhibo Chen. End-to-end rate-distortion optimized 3d gaussian representation, 2024a. URL https://arxiv.org/abs/2406.01597.

Jiaping Wang, Peiran Ren, Minmin Gong, John Snyder, and Baining Guo. All-frequency rendering of dynamic, spatially-varying reflectance. *ACM Trans. Graph.*, 28(5):1–10, December 2009. ISSN 0730-0301. doi: 10.1145/1618452.1618479. URL https://doi.org/10.1145/1618452.1618479.

Yiwen Wang, Siyuan Chen, and Ran Yi. Sg-splatting: Accelerating 3d gaussian splatting with spherical gaussians, 2024b. URL https://arxiv.org/abs/2501.00342.

Yufei Wang, Zhihao Li, Lanqing Guo, Wenhan Yang, Alex C. Kot, and Bihan Wen. Contextgs: Compact 3d gaussian splatting with anchor level context model, 2024c. URL https://arxiv.org/abs/2405.20721.

Shuzhao Xie, Weixiang Zhang, Chen Tang, Yunpeng Bai, Rongwei Lu, Shijia Ge, and Zhi Wang. Mesongs: Post-training compression of 3d gaussians via efficient attribute transformation, 2024. URL https://arxiv.org/abs/2409.09756.

Jiahui Zhang, Fangneng Zhan, Ling Shao, and Shijian Lu. Sogs: Second-order anchor for advanced 3d gaussian splatting, 2025a. URL https://arxiv.org/abs/2503.07476.

Yangming Zhang, Wenqi Jia, Wei Niu, and Miao Yin. Gaussianspa: An "optimizing-sparsifying" simplification framework for compact and high-quality 3d gaussian splatting. In *Proceedings of the Computer Vision and Pattern Recognition Conference (CVPR)*, pp. 26673–26682, June 2025b.

Zhaoliang Zhang, Tianchen Song, Yongjae Lee, Li Yang, Cheng Peng, Rama Chellappa, and Deliang Fan. Lp-3dgs: Learning to prune 3d gaussian splatting, 2024. URL https://arxiv.org/abs/2405.18784.